

IN SITU INVESTIGATION OF SLIDING DIRECTION DEPENDENCY ON THE WEAR
OF SINGLE CRYSTAL MAGNESIUM OXIDE

By

KELLON RYAN MARCHMAN

A THESIS PRESENTED TO THE GRADUATE SCHOOL
OF THE UNIVERSITY OF FLORIDA IN PARTIAL FULFILLMENT
OF THE REQUIREMENTS FOR THE DEGREE OF
MASTER OF SCIENCE

UNIVERSITY OF FLORIDA

2012

© 2012 Kellon Ryan Marchman

To my parents, Ken and Rhonda Marchman, my brother, Alan Marchman, and my wife,
Jacquelyn Marchman for their lifelong encouragement, advice, and inspiration

ACKNOWLEDGMENTS

I would like to thank my graduate advisor Dr. W.G. Sawyer for sharing his wealth of knowledge through his teaching and mentoring, and for sharing numerous life-enriching experiences with me over the past three years. I would also like to thank the members of my committee, Dr. Tommy Angelini and Dr. Peter G. Ifju for their time and teaching efforts through my tenure at the University of Florida.

I would like to thank my loving and encouraging wife Jacquelyn Marchman for her support, patience, and encouragement while finishing this research.

I would like to extend a special thank you to my colleague Dr. Brandon A. Krick for his help and support throughout my time in the University of Florida Tribology Laboratory. A thank you also goes to Ira Hill who aided me in automating some data retrieval for this work. I would like to thank Dr. Perry and Xueying Zhao for their help with crystallographic analysis.

I would also like to thank both current and former members of the University of Florida Tribology Laboratory for their collaborations and encouragement through my term.

TABLE OF CONTENTS

	<u>page</u>
ACKNOWLEDGMENTS.....	4
LIST OF TABLES.....	6
LIST OF FIGURES.....	7
CHAPTER	
1 INTRODUCTION	10
Experimental Practices-Tribometry.....	10
Magnesium Oxide: A Brief Overview and Previous Studies.....	12
Magnesium Oxide	12
Relevant Previous Studies	13
Optical Interferometric Profilometry	16
Summary of Research	17
2 EXPERIMENTAL METHODS	18
Overview of Tribometer.....	18
Sample and Load Positioning.....	18
Normal and Friction Force Measurement	19
<i>In Situ</i> Optical Profilometry	22
Data Acquisition and Scan Automation	22
Environmental Control.....	23
Sample Selection	23
Experimental Techniques	24
Uncertainty in Measurements	25
3 EXPERIMENTAL RESULTS AND DISCUSSION.....	26
4 CONCLUSIONS	39
APPENDIX	
A UNCERTAINTY ANALYSIS.....	40
Uncertainty in Coefficient of Friction Measurements.....	40
Uncertainty in Wear Rate Measurements	42
B RESOLVED SHEAR STRESS CALCULATIONS	45
LIST OF REFERENCES	47
BIOGRAPHICAL SKETCH.....	50

LIST OF TABLES

<u>Table</u>		<u>page</u>
2-1	Uncertainty analysis calculations for friction coefficient measurements	25
2-2	Uncertainty analysis calculations for wear rate measurements of MgO	25
3-1	Testing parameters used	29
A-1	Uncertainty analysis calculations for friction coefficient measurements	44
A-2	Uncertainty analysis calculations for wear rate measurements of MgO	44

LIST OF FIGURES

<u>Figure</u>	<u>page</u>
1-1 MgO has a simple cubic close packed structure that is easy to model but provides substantial wear resistance.....	13
1-2 Schematic of the light paths and components of scanning white light interferometry. Adapted from [23]......	17
2-1 Illustration of the tribometer used for this study.	18
2-2 Exaggerated Leaf spring flexure deformation. Axes used for stiffness calculations are shown.	20
3-1 Friction coefficient, μ , shown as a function of track location in degrees. This plot shows fairly isotropic friction values over the length of the track.....	26
3-2 The distribution of normal force imposed as a function of the track location in degrees.	28
3-3 A schematic showing the locations of the scans around the wear track. Representative profile scans of the wear track are displayed. Each rectangle on the track represents the scaled spatial size of the scan (583 x 437 μ m).	31
3-4 A typical cross-sectional profile of the wear track of MgO. Additionally, how area loss determinations were made.....	31
3-5 Anisotropic wear behavior of single crystal MgO expressed as a function of the angular position, measured from the center of the wear track. The black arrows represent the family of sliding direction at that position. Directions were verified by LEED.	32
3-6 Slip plane notations	35
3-7 The resolved shear stresses as a function of sliding direction on the (100) plane. The solid path represents the magnitude between the different slip planes. This trend follows perfectly with the wear rate trend seen above.	36
3-8 The severity of the plastic deformation rapidly increases over a relatively short period of sliding. The cracks began to propagate at approximately 3700 cycles.	37
3-9 A comparative and control test to the MgO results above. The ionic crystalline structure produces similar dependency results while the amorphous glass shows constant wear.....	38
A-1 Misalignment error in surface normal direction. Measured via optical techniques.	42

B-1 The notations used in the resolved shear stress calculations. The F_f vector is held constant and θ is swept along 360 degrees for each of the four active slip planes..... 45

Abstract of Thesis Presented to the Graduate School
of the University of Florida in Partial Fulfillment of the
Requirements for the Degree of Master of Science

IN SITU INVESTIGATION OF SLIDING DIRECTION DEPENDENCY ON THE WEAR
OF SINGLE CRYSTAL MAGNESIUM OXIDE

By

Kellon Ryan Marchman

May 2012

Chair: W.G. Sawyer
Major: Mechanical Engineering

Ionic solids are unique materials to study, offering a wide range of physical properties and varying crystallographic tendencies. Amongst this group is magnesium oxide (MgO). Magnesium oxide is a well suited ceramic in tribological testing due to its relatively high hardness, high melting temperature, and its simple cubic crystal structure. In this study, the effect of crystallographic direction on MgO's wear rate is examined. A pin-on-disk tribometer is combined with a scanning white light interferometer to provide profilometry scans of the wear track for wear rate measurements. The final wear result was determined after a sliding distance of 180 meters using a normal load of 1 Newton in a dry nitrogen environment: a distinct sinusoidal relationship between the wear rate and angular position of the wear track exists. This is indeed due to anisotropy of the material in different crystallographic directions. It is proposed that a main contributor to this phenomenon is the varying distribution of the resolved shear stress along the slip planes of the crystal. To test this result and its application to single crystal ionic solids, sodium chloride was also tested, as well as an amorphous glass specimen. A similar trend was found in sodium chloride whereas no such trend manifested itself in the noncrystalline glass sample.

CHAPTER 1 INTRODUCTION

Dynamically interacting solid body surfaces are inherently deleterious to the life of the body unless measures are taken to reduce the wear and friction occurring at their interface. The deformation of the solid body over a progression of cycles is known as wear. This deformation occurs due to high contact pressures present during sliding. These high contact pressures are caused by the microscopic contact areas of asperities, or peaks found on a nominally flat surface, with the interacting surface [1]. For these reasons, contact mechanics of rough surfaces are of great importance in tribological wear and friction studies [2].

Experimental Practices-Tribometry

Tribological properties such as friction coefficients and wear rates are very important parameters to consider in engineering design. High friction coefficients can lead to minimal efficiency in dynamic systems and also increase the wear of components. With increasing wear, numerous wear debris particles are generated which can inhibit the function of surrounding operations thus leading to a very short life span. Tribometry embodies the associated experimental techniques and methods necessary for quantifying these important design parameters.

The friction coefficient, μ , is defined as the ratio of the friction force to the normal force. Due to the asperity contacts as discussed previously, the magnitude of the normal and friction forces are defined as the sum of the forces present at the asperities. There are numerous tools available for obtaining the desired normal force. Some common tools include dead weight loads, piezoelectric driven cantilevers, and linear

stages. The friction forces can be measured with linear force transducers or displacement monitoring devices such as capacitance probes. A typical tribometer configuration for such friction testing is a spherical pin on a large flat surface, or counterface. The pin material is chosen based on properties of high hardness and an ideally smooth surface in order to concentrate both the friction and wear on the counterface, the material of interest. The uncertainties associated with friction coefficient measurements are of importance and detailed studies have been done by Schmitz *et al.* [3] for linearly reciprocating pin-on-flat tribometers and Krick *et al.* [4] for pin-on-disk rotary tribometers.

The deformation that occurs due to sliding can be measured by the wear volume of the specimen. A relationship that expresses the wear rate of a material in a tribosystem has been defined by Archard and can be reduced to:

$$K = \frac{W}{sP} \quad (1-1)$$

where K is the wear rate (typically expressed in units of $\text{mm}^3/(\text{Nm})$), s is the sliding distance in, P is the applied normal load, and W is the volume lost due to wear [5].

Volume loss can be measured by mass loss as well as optical scanning techniques. It is important, however, to understand the amount of uncertainty associated with volume loss measurements, as this directly correlates to the quality of the calculated wear rate. Schmitz *et al.* defines the uncertainty of a reciprocating pin-on-flat for mass loss based wear rate calculations [6]. Surface scanning techniques are becoming increasingly common forms of volume loss measurements due to their high precision and ease of implementation. For relatively large wear tracks, however, it is difficult to examine the

entire wear track due to the limited spatial resolution of surface scanning devices. To avoid this problem for circular wear tracks, it is acceptable to scan the wear track in subsections at constant intervals. This technique invokes uncertainty due to the non-uniformity of the wear track caused by variations in the applied load [7]. Colbert *et al.* discusses the importance of the number of scans necessary in order to reduce the uncertainty of the measurement to an acceptable level [8].

Magnesium Oxide: A Brief Overview and Previous Studies

Single crystal ionic solids are of interest in this study because of their natural formation habits and interesting mechanical properties. Ionic solids exhibit the high strength of chemical bonding due to the large electronegativity difference between their two oppositely charged ions. Ionic solids can have numerous crystallographic structures but one common factor is that most have close packed atoms. This efficient packing means that the cations will tend to fill a hole that is slightly smaller than itself. This is necessary in order to prevent the larger like-charge anions from contacting each other.

Magnesium Oxide

Single crystal magnesium oxide (MgO) is an ionic solid ceramic that exhibits high melting temperature and relatively high hardness values of $T_m \approx 2800^\circ\text{C}$ and $HV \approx 910$, respectively. Magnesium oxide also exhibits a high elastic modulus and yield strength, allowing higher contact stresses to be attained while avoiding excessive deformation [9]. It is a valuable material to study because of these desirable physical properties and its simple crystal structure. The crystal structure of MgO is that of rock salt, which has a face-centered-cubic lattice structure as seen below in Figure 1-1. The magnesium

cations fill the octahedral holes in the lattice since the ionic radii ratio of magnesium cations to oxygen anions ($r_{\text{cation}}/r_{\text{anion}}$) is 0.683, which is too large for tetrahedral holes and too small for cubic holes. Rock salt structure cleavage is well known and occurs along the (100) plane.

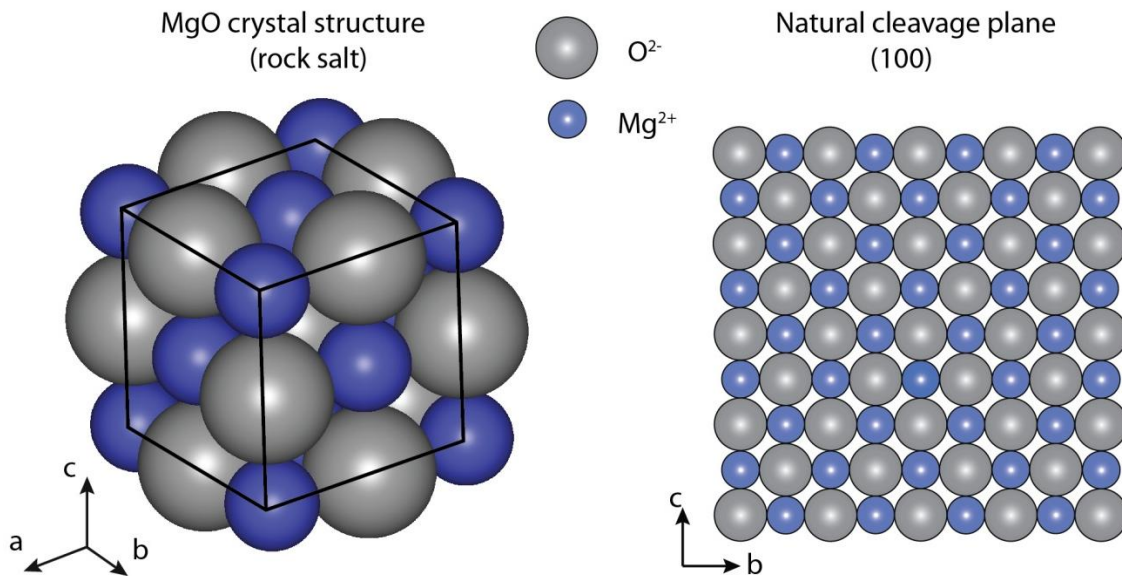


Figure 1-1. MgO has a simple cubic close packed structure that is easy to model but provides substantial wear resistance.

Relevant Previous Studies

Wear studies on single crystal MgO date back to the 1960s and most were focused on understanding the brittle fracture and subsurface dislocation movements of MgO under wearing environments [9-13]. R.J. Stokes suggested that in some ceramics, although brittle fracture occurs, plastic deformation can also occur at low temperatures and relatively low stresses [11]. This notion was validated by R.P. Steijn in 1963 when he investigated the subsurface damage of ionic crystals due to rubbing [12]. Steijn conducted scratch tests on single crystal MgO and used etching techniques to verify dislocation movements around the scratch track. He found that the glide motions were

consistent with that of rock salt's slip systems, which are along the dodecahedral plane. Studies verifying these dislocation movement and slip plane results with electron transmission microscopy have been completed by J. Washburn *et al.*[14]. Further work on dislocation motion was done by Stokes *et al.* on the dislocation movement of MgO and methods of locking dislocation movement in single crystals [10]. Stokes was able to correlate some of the dislocation locking to the anisotropic plasticity of MgO.

Studies were conducted on sliding speed and load dependency of wear in MgO on steel by Sugita *et al.*[15]. Sugita found that as sliding speed increased, both the wear on the MgO single crystal slider and the steel disk decreased. He attributed this trend to a diffusion process occurring at the interface of the sliding and a reduction in the amount of brittle fracture caused by lower sliding speeds. Amateau *et al.* and Dufrane *et al.* investigated the effect of rolling stresses on single crystal MgO [9, 16]. Amateau confirmed that plastic deformation incurred on the MgO sample was attributable to stresses which were similar to those calculated using Hertzian contact pressures for elastic conditions. Dufrane's work drew a dependence of slip depth on rolling velocity in single-pass experiments based on the dependence of dislocation velocities due to applied stresses.

In 1966, F.P. Bowden and A.E. Hanwell experimented with the friction of clean single crystal surfaces in very high vacuum (10^{-10} torr) to examine the effects of tenacious surface contaminant layers on their frictional behavior [17]. Bowden experimented with single crystal MgO sliding on itself in specifically oriented crystallographic directions (sliding occurred in the [100] direction). It was found that by removing the layer of adsorbed gasses from the surface, the friction coefficients are

greatly increased due to a lack of lubricious monolayers of oxygen and water. The contaminant layers were removed from the surface due to the rubbing action and due to the high vacuum, the recontamination rate is greatly reduced. Due to the interface of the clean surfaces, the friction is dominated by adhesive forces at the junction. The adhesion seen at the interface is directly related to the inherent interatomic bond strengths of the material.

In a later study, Bowden *et al.* also investigated the frictional anisotropic behavior of MgO with a dependence on sliding direction [18]. Bowden found that the friction of single crystals of MgO did not depend on sliding direction if the sliding conical tip was of an angle greater than 150° (i.e. blunt or spherical tipped sliders). Knoop hardness tests were conducted with the long axis of indentation aligned in different crystallographic directions. Bowden discovered that there is a hardness dependency on direction and that the hardness of the $\langle 100 \rangle$ family of directions is approximately half the value of the $\langle 110 \rangle$ directions. Bowden also found that the wear behavior of MgO produced chevron type cracks in the area directly surrounding the wear track. Through this study and previous efforts, it was deduced that these chevron patterns were formed due to dislocations occurring sub-surface in response to sliding. These are the same patterns that were found by Steijn [12] as discussed above.

In situ tribology is a subset of tribological testing techniques that can be used for many purposes. Sawyer et al. used *in situ* profilometry and a linear reciprocating tribometer to understand the morphology of MoS₂ friction and wear [19]. Argibay et al. used *in situ* methods to analyze sliding electrical contacts as a function of brush type and current densities [20]. In [21] Wahl and Sawyer discuss the multiple applications for

using *in situ* techniques. They discuss how integrating *in situ* instrumentation can allow for tribologically interesting events can be correlated with physical effects of such changes

Optical Interferometric Profilometry

This method of surface profilometry is widely used in the metrology field due to its non-destructive nature and ease of application. Vertical scanning white light interferometers (SWLI) are common forms of this type of profilometer. For most applications, these interferometers use a Mirau interferometer coupled with a charge-coupled device (CCD) image sensor to provide a topographical representation of a sample surface [22]. A short coherence length light source projects a white light into a semi reflective beam splitter. One arm of the split beam is incident on a reference mirror and the other is incident on the testing sample. By varying the interferometer height with a piezoelectric transducer, constructive and destructive interference fringes are created between the reflected split beams. These interference fringes are projected onto the CCD, which converts the image into a digital array for further analysis by software. These types of interferometers can have vertical resolutions of a few nanometers and lateral resolutions as low as 0.5 μm /sample, depending on the diffraction limit of the light used and the magnification. Figure 1-2 depicts the light path of a SWLI similar to the model used for this study.

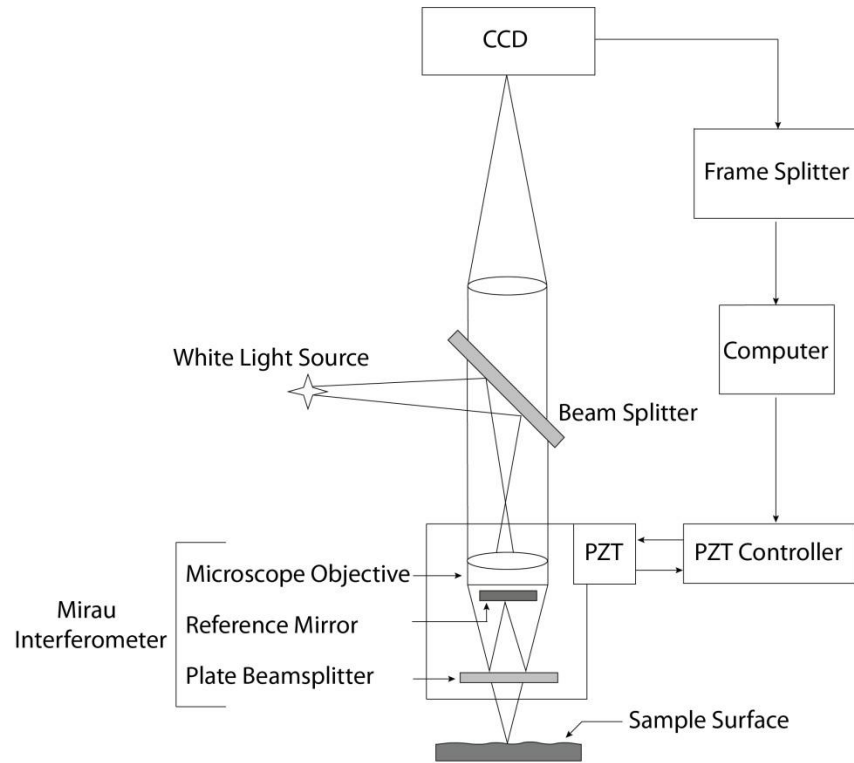


Figure 1-2. Schematic of the light paths and components of scanning white light interferometry. Adapted from [23].

Summary of Research

In previous ionic solid research conducted over my term, interesting wear behavior manifested itself for numerous samples. One sample in particular that showed interesting wear was MgO. This study aims to further investigate the roles of crystallographic structure, ionic bond strength, and sliding direction on the wear of MgO. A pin-on-disk tribometer is instrumented with a double leaf flexure and combined with a scanning white light interferometer for macroscopic wear testing and *in situ* wear track examination. A correlation with the anisotropic hardness findings of Bowden, as discussed above, and wear rate is anticipated. This work will discuss the experimental techniques, mathematical methods, and data acquisition necessary to explore this hypothesis.

CHAPTER 2 EXPERIMENTAL METHODS

Overview of Tribometer

The tribometer used for this study is a custom adaptation of the in-situ tribometer as described by Keith [24]. This tribometer is a pin-on-disk apparatus that has the ability generate a wear experiment while simultaneous monitoring the evolution of wear.

Figure 2-1 illustrates the tribometer componentry and layout as adapted for use in this work.

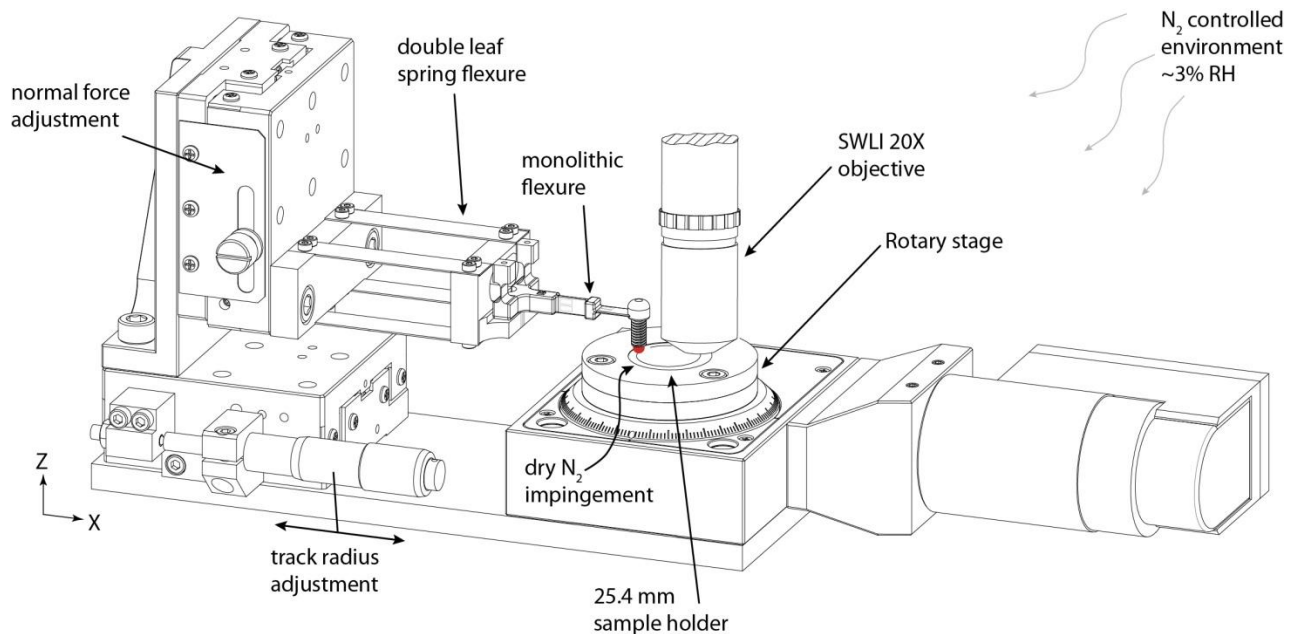


Figure 2-1. Illustration of the tribometer used for this study.

Sample and Load Positioning

Sample positioning was accomplished via a Physik Instrumente (PI) M-060-PD precision rotary stage controlled by a PI Mercury C-863 controller. The stage incorporates a direct current drive servo motor with a worm gear reduction. The sample was rigidly attached to the stage using a clamp mechanism. The stage is capable of

rotation speeds up to 90 deg/s and a unidirectional repeatability of 50 μ rad. Position feedback was accomplished via a rotary encoder with a resolution of 0.0018 degrees.

Wear track and force adjustments were achieved by OptoSigma linear ball bearing stages mounted orthogonally in the X and Z directions. The stages are micrometer driven with a resolution of 10 μ m. The resolution provided by these stages ensured an accurate wear track radius position and normal force application.

Normal and Friction Force Measurement

This tribometer uses a 304 stainless steel monolithic biaxial force transducer to measure both the friction and normal forces [25]. To compensate for sample leveling inaccuracies and to aid in providing a constant normal force, a double leaf spring flexure was incorporated into the tribometer design. The double stacked parallelogram leaf spring configuration increased the torsional rigidity and limited out-of-plane rotations. The leaf spring flexure stiffness values were calculated using equations 2-1 through 2-3 [26] using the axes notations shown in Figure 2-2.

$$K_{\delta_z, F_z} = 2Eb \left(\frac{t}{L} \right)^3 \quad (2-1)$$

$$K_{\delta_y, F_y} = \frac{btG}{1.5L} \quad (2-2)$$

$$K_{\theta_x, F_x} = \frac{Eb^3t}{L^3} \left(1 + \frac{1.5Eb^2}{GL^2} \right)^{-1} \quad (2-3)$$

The stiffness in the normal direction (K_{δ_z, F_z}) was calculated to be ~3.5 N/mm, while the stiffness in the lateral direction (K_{δ_y, F_y}) was three orders of magnitude higher at ~8,300

N/mm. The torsional rigidity about the x-axis (K_{θ_x, F_x}), as defined below in Figure 2-2, was calculated to be eight orders of magnitude higher than the normal stiffness at $\sim 8.8 \times 10^8$ N·mm/rad. These values indicate that the flexure assembly was well suited for only normal plane displacements with relatively low loads. Finite element analysis based simulations were also carried out and showed supportive values to the calculated values above.

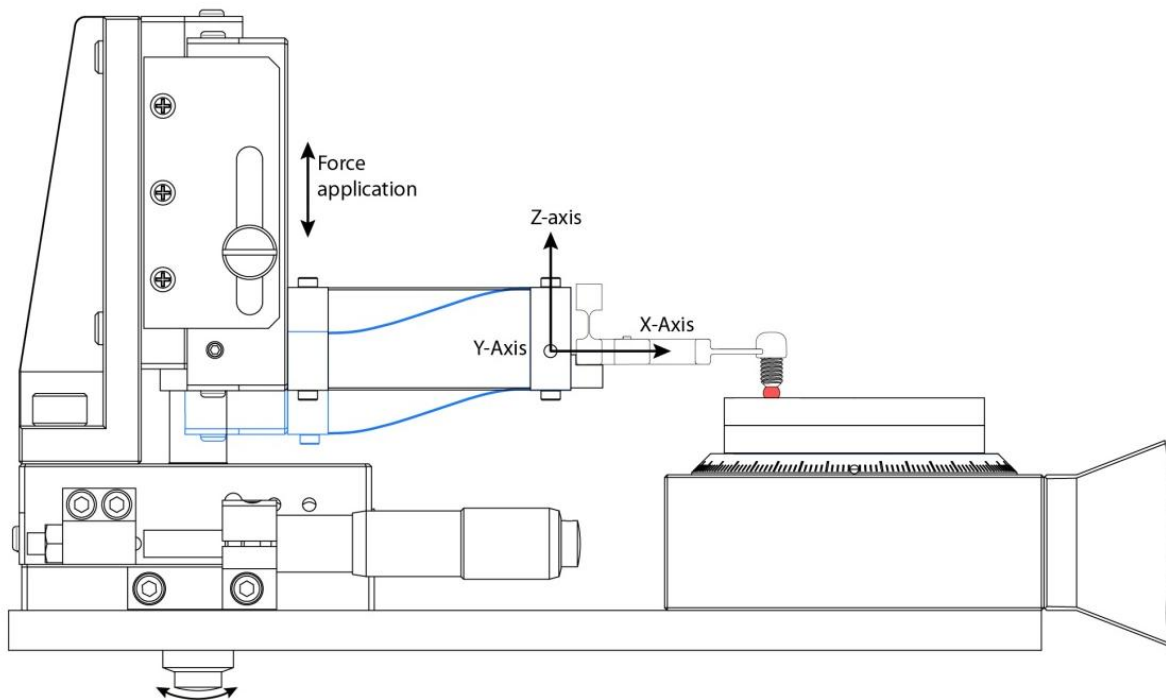


Figure 2-2. Exaggerated Leaf spring flexure deformation. Axes used for stiffness calculations are shown.

The monolithic flexure uses two full strain gage Wheatstone bridges for both the normal and the lateral force measurements. There are two gages on each side of the flexure for each measurement. The full bridge configuration provides temperature compensation to the circuit and aids in preventing crosstalk between the signals. The gages are placed on the flexure at points furthest from the loading in order to increase sensitivity. The transducer is paired with Sensotec UV-10 in line amplifiers to provide

direct current excitation voltage and conditions the gage outputs to be read by the data acquisition card. Using the same notation above, the normal force stiffness (K_{δ_z, F_z}) and lateral stiffness (K_{δ_y, F_y}) of the monolithic flexure were found to be an order of magnitude higher than those of the leaf flexure at 71.4 N/mm and 19.0 N/mm, respectively. Furthermore, experimental stiffness calculations were carried out on the entire flexure assembly. With known displacements induced on the vertical axis, the measured forces were recorded and a linear fit applied to the data. The composite stiffness for the assembly of the leaf flexure and monolithic flexure was 3.07 N/m. This value is very close to the calculated normal direction stiffness for the leaf flexure as shown above, indicating that the monolithic flexure is considered mostly rigid in the system. The combination of this stiff flexure with the compliant leaf spring flexure ensures that the desired normal force is imposed on the sample and remains mostly constant through the wear track path.

Prior to starting experiments on an instrument, it is essential to calibrate the strain reading flexure to obtain the calibration constant that can be used to back out forces. To calibrate the flexure assembly, the 90 degree angle bracket that the flexure assembly is mounted to was removed from the tribometer and bolted to an optical table for rigidity. Known masses were then hung from the cantilever and voltage shifts incurred by the Wheatstone bridge were recorded. The flexure was calibrated up to two times the target nominal force to provide an acceptable range of calibration data. The process was repeated with the flexure rotated 90 degrees to calibrate the tangential direction stiffness. A linear fit was imposed on the data for both the normal and tangential directions and values were recorded as -1.637 N/V and 0.67 N/V, respectively.

***In Situ* Optical Profilometry**

The optical profilometry is provided by a Veeco Wyko NT9100. The positioning of the profilometer was opposite the side of the pin such that the pin was unloaded from the sample and the sample can be scanned around its entire track. After each cycle interval, the disc was rotated in increments of 6 degrees and scanned, for a total of 60 optical profile measurements. The profilometer was set in vertical scanning interferometry (VSI) mode. This mode allows for large step sizes to be resolved while still keeping a vertical height resolution of around 3-5 nm with lateral spatial resolution of 0.5 μm /sample. The instrument was equipped with a 20X Mirau objective and imaged using a field of view (FOV) of 0.55X for a magnification of height values of approximately 11X. The measurement field for a single scan on MgO was 583 μm by 437 μm .

Data Acquisition and Scan Automation

Wired connections were passed through a National Instruments SCB-68 connector block and data acquisition was handled through a National Instruments PCI-6621 16-bit card. The controls programming and data storage was accomplished through LabVIEW. The acquisition rate of the force data was set to sample at a rate of 1 kHz, at which the position data from the rotary stage were also recorded. The data were averaged every second and combined with rotary position of its associated acquisition cycle. At every cycle stop interval, a total of 60 equally spaced optical profilometry scans were taken around the wear track, which was automated for efficiency. Once the prescribed cycle interval was completed and the pin was unloaded, the automation routine commanded the stage to rotate to a set number of degrees before commanding the SWLI computer

to activate a new scan. Once the scan is complete, the scan dataset was saved and the process was repeated.

Environmental Control

Many ionic crystals, such as NaCl and MgO, are largely hygroscopic. This means that the adsorption of water molecules greatly effects the physical and chemical properties of the sample [27]. To avoid this, a dry environment was established through an impingement of dry nitrogen gas onto the surface, which was then enveloped by a local environmental control container. The relative humidity recorded after a brief purge period was approximately 3% RH. The relative humidity measurement was made by an Omega Thermo-Hygrometer (model number RH411). The flow of nitrogen was reduced once the volume was purged and was kept constant through the entirety of the testing.

Sample Selection

Optical window samples were chosen as the running surface for this study because of their superior flatness and exceptionally smooth polished surfaces. Prior to testing, surface roughness measurements were taken of the MgO optical windows obtained from Crystran and averages were below $R_a = 2\text{nm}$. All samples tested were 25mm diameter disks of thicknesses between 2 and 3 mm.

For this study, chromium oxide doped sapphire (synthetic ruby) ball lenses 3.18 mm in diameter served as the pin. Pre-test SWLI surface scans of the ruby ball showed a radius of curvature of approximately 1.60 mm and a surface roughness, R_a , of $\sim 4.5\ \mu\text{m}$. Ruby has a hardness that is approximately 2.5 times greater than MgO with Vicker's hardness measurements of ~ 2300 and ~ 910 , respectively. The ruby ball lens was set on the end of a cup point set screw using a fast acting cyanoacrylate adhesive.

Experimental Technique

In order to successfully record the data necessary for tracking the sample's wear rate based on the azimuthal position, several experimental steps are essential. Once the sample was clamped into the sample holder, the SWLI objective was placed over the position at which the wear track would evolve. This location was determined by using the known geometries of the sample holder and the calibrated wear track diameter. The pin was then lowered into contact with the sample and the normal force was set based on the 1000 Hz data displayed on the DAQ computer. Once the desired normal force was acquired, the next step was to set up the testing parameters on the DAQ computer. The experiments were completed such that the wearing event would take place for a defined increment of sliding cycles (a sliding cycle is one 360 degree rotation), after which the pin would be unloaded from the sample and the scanning cycle would commence. The scanning process was automated such that the sample would rotate six degrees, pause for approximately 20 seconds until the instrument completed the scan and saved the data, and then the sample would rotate another six degrees and repeat the process until the sample was rotated 360 degrees (one scanning cycle). A total of 60 scans around the entire wear track were completed using this method. With the automated routine, one scanning cycle's interval was approximately 30 minutes. Once the scanning cycle was completed, the pin was reloaded onto the surface making sure to achieve the same normal load, without having to dismount the sample or adjust the wear track position. A total of 1800 wear track scans were taken over the 3000 cycle test.

Uncertainty in Measurements

It is very important to develop an uncertainty analysis to validate the reported results of experimental data. In tribological testing systems, uncertainties in wear rates and friction coefficients can stem from numerous sources but typically the largest source of uncertainty is derived from the precision of the instrument. Much work has been done in this area in an attempt to minimize these uncertainties and maximize the quality of experimental measurements. Uncertainty analysis methods described by multiple previous studies [3, 6, 8] are employed here to assess the quality of data supplied in this work. A complete method for calculating the uncertainties is provided in Appendix A, with summarized values in Tables 2-1 and 2-2. The uncertainty in the wear rate ranged from 3% for high volume loss to 8% for low volume losses.

Table 2-1. Uncertainty analysis calculations for friction coefficient measurements

Parameter	Nominal Value	Standard uncertainty	Sensitivity,	Contribution
		$u(x)$	$\frac{\partial \mu}{\partial x}$	(%)
F_N (N)	1.01	0.025	0.20	5.65
F_T (N)	0.202	0.004	0.99	94.35
Combined standard uncertainty u_c			4.0×10^{-3}	

Table 2-2. Uncertainty analysis calculations for wear rate measurements of MgO

Parameter	Nominal Value	Standard uncertainty	Sensitivity,	Contribution
		$u(x)$	$\frac{\partial \mu}{\partial x}$	(%)
F_N (N)	1.01	0.025	0.20	25.34
V_{loss} (mm ³)	1.3×10^{-4}	5.61×10^{-6}	5.5×10^{-3}	74.65
d (m)	180	1×10^{-8}	4.08×10^{-9}	0
Combined standard uncertainty u_c			3.6×10^{-8}	

CHAPTER 3 EXPERIMENTAL RESULTS AND DISCUSSION

As discussed previously, Bowden *et al.* found that the friction coefficient of single crystal MgO manifested anisotropic behavior for conical pin sliders with angles less than 150 degrees but became much more isotropic with blunt pins. With sharp indenters, Bowden found that the friction coefficient, μ , would increase by as much as three times between “low” and “high” friction sliding directions. According to this finding, a hemispherical pin should provide fairly isotropic friction behavior regardless of the sliding direction. Friction coefficient as a function of the track location angle is shown below in Figure 3-1.

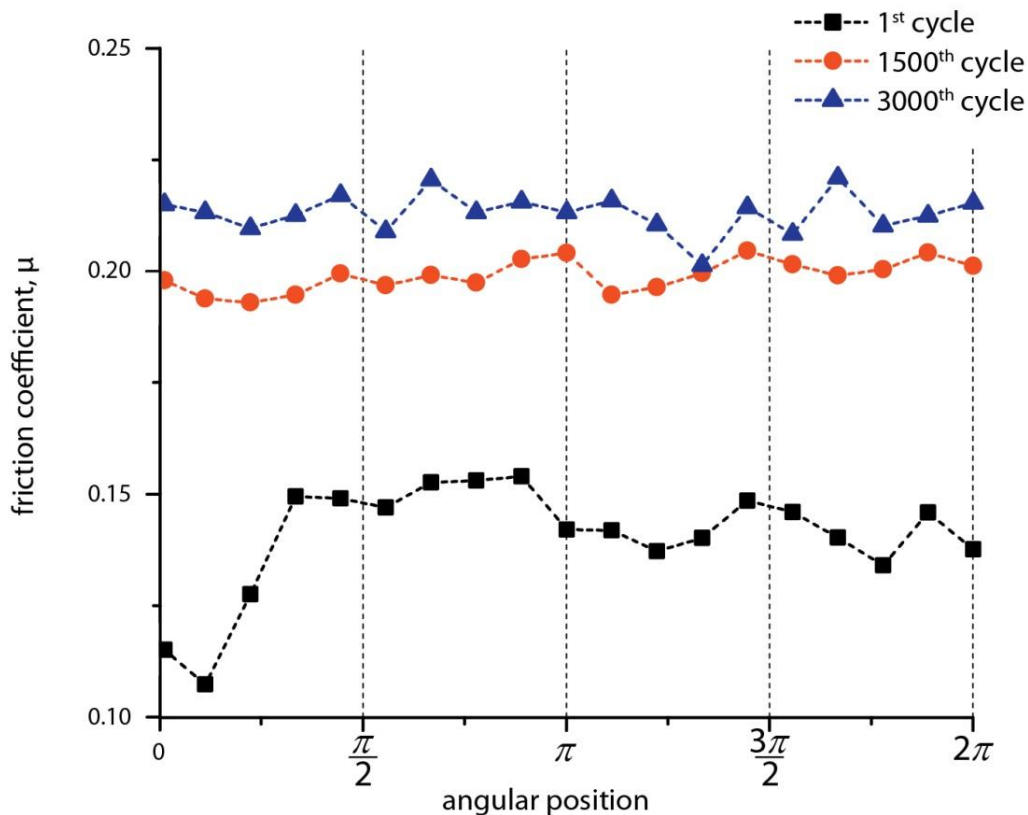


Figure 3-1. Friction coefficient, μ , shown as a function of track location in degrees. This plot shows fairly isotropic friction values over the length of the track.

Figure 3-1 verifies that μ remains relatively constant throughout the circumference of the wear track. This consistency is important to the wear study in this work. A constant friction force imposes a constant and uniform shear stress distribution along surface of the track, which provides equal opportunity for a wear event to occur at every location along the track. Thus, any wear accumulated by the process is only attributable to the material properties instead of varying load conditions. Since the μ values above were calculated based the ratio of friction force to normal force as shown here,

$$\mu = \frac{F_T}{F_N} \quad (3-1)$$

it is also very important to maintain a constant normal force along the circumference of the wear track.

A conservative normal force of 1 N was selected for these tests in an attempt to minimize brittle fracture of the specimens. With a nominally normal load of 1 N and a ruby spherical pin with a radius of 1.5875 mm, the Hertzian contact pressure for the interface was calculated to be approximately 1160 MPa. With a reported compressive strength value for MgO of 2400 MPa, the contact pressure using the above parameters is less than 50% of the compressive strength of MgO.

Figure 3-2 below shows the distribution of normal forces along the circumference of the track for several cycles. Spatially resolved position data were acquired from the stage's rotary encoder output synced with force data recorded by the transducer. The normal force data is plotted in 20 degree increments in order to provide an accurate representation of how the normal force varies. Averaging all of the normal force position data yielded an average F_N of 1.01 N. The standard deviations of the normal force for

several cycles were calculated and the average of these deviations per cycle was a low 0.006 N. Furthermore, an average peak to peak normal force value was found to be approximately 0.03 N. This normal force uniformity means that axial run out deviations are minimized, thus reducing the associated uncertainties as discussed the following section. The reduction of the normal force variation was achieved by a combination of leveling techniques, parallel testing samples, and implementation of a compliant flexure.

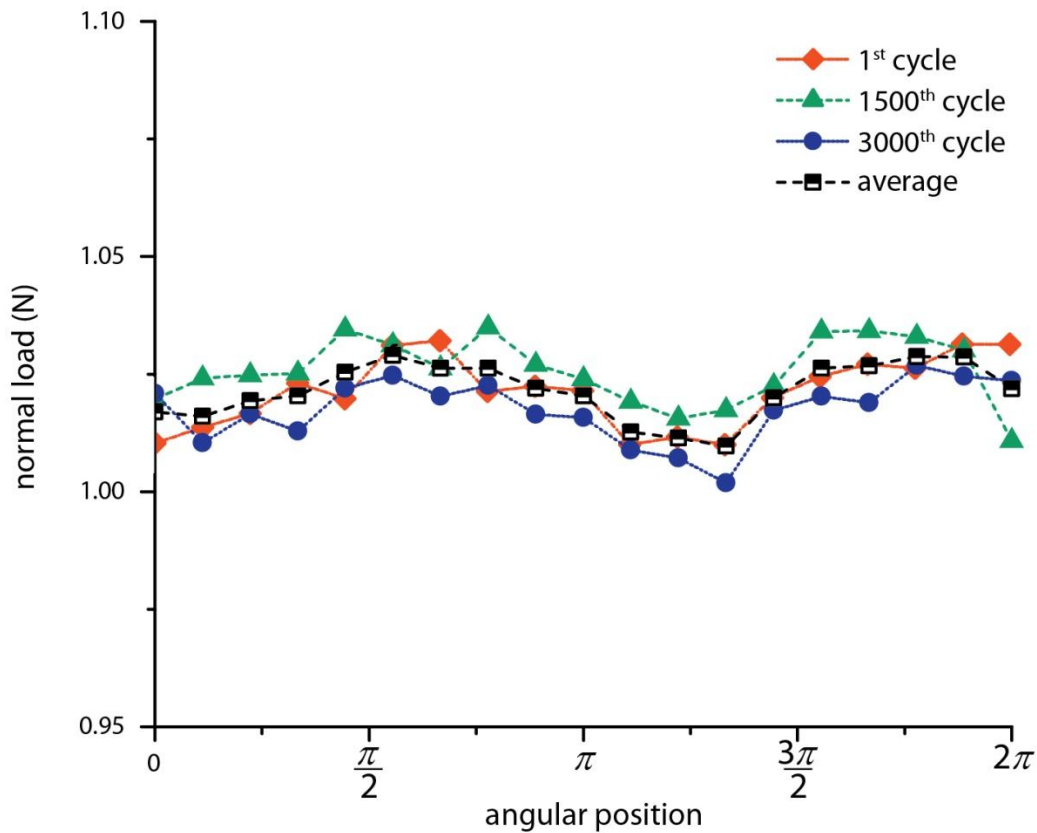


Figure 3-2. The distribution of normal force imposed as a function of the track location in degrees.

As discussed previously, the friction and normal forces were obtained using a monolithic cantilever transducer with a leaf spring flexure. The transducer and the conditioner pair output a voltage that is multiplied by stiffness coefficient determined for

the flexure in order to obtain the force acting on the flexure. The equations used to calculate the normal and friction force are shown below in equations (3-2) and (3-3), respectively.

$$F_N = C_N V_N \quad (3-2)$$

$$F_T = C_T V_T \quad (3-3)$$

In the above, C represents the calibration constant for the flexure in N/V, and V is the output voltage of the signal conditioner. The subscripts N and T represent the normal and tangential direction, respectively.

Of great importance in this study is the determination of MgO's wear rate over a given number of cycles. The wear studies in this work were carried out using the testing parameters summarized below in Table 3-1.

Table 3-1. Testing parameters used

Parameter	Values
Applied nominally normal load (F_N)	1 N
Nominal contact pressure	1160 MPa
Speed (angular(ω), linear(v))	71 deg/s, 12 mm/s
Number of cycles (N),	3000
Sliding distance (d)	180m
Nominal wear track diameter (D)	19mm
Relative humidity	3%
Cover gas	Dry nitrogen

For calculating the wear rate, the above parameters and geometries can be implemented based on equation (1-1).

$$K = \frac{V_{loss}}{F_N d} \quad (3-4)$$

In order to determine the volume loss by wear, several steps were taken. At each six degree increment along the track, an optical scan was taken of the wear track. The process was automated such that once the scan finished, the dataset was saved, the stage was rotated another six degrees, and the process was repeated. Figure 3-3 depicts the scanning increments around the disk, as well as representative wear track profile scans. The wear track was centered in the image such that a profile line scan would pass through the track at the specified degree interval and normal to the tangential direction. With line scans obtained for each degree interval, the data were then processed in Matlab to calculate the area below the surface that is contained by the wear track. Use of the trapezoidal integration rule was implemented to determine this area loss. To obtain the volume loss, the area loss was then integrated along the circumference of the track. A representative line scan of the MgO wear track is shown below in Figure 3-4. The dimensions of the track, however, are not constant at every scan location. Since such little wear occurred after 3000 cycles the wear track width was not always explicitly clear. For each profile scan, the wear track width was chosen by referencing the profile data with the original optical scan taken by the SWLI. This way, the correct points were chosen to integrate under for each scan thus minimizing uncertainties in the area calculations.

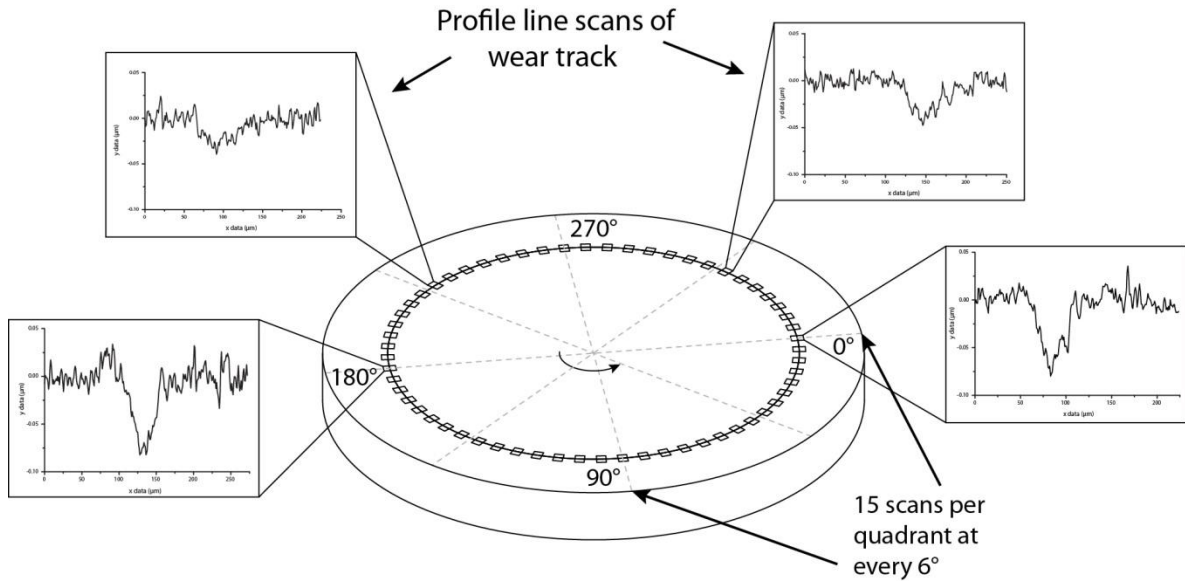


Figure 3-3. A schematic showing the locations of the scans around the wear track. Representative profile scans of the wear track are displayed. Each rectangle on the track represents the scaled spatial size of the scan (583 x 437µm).

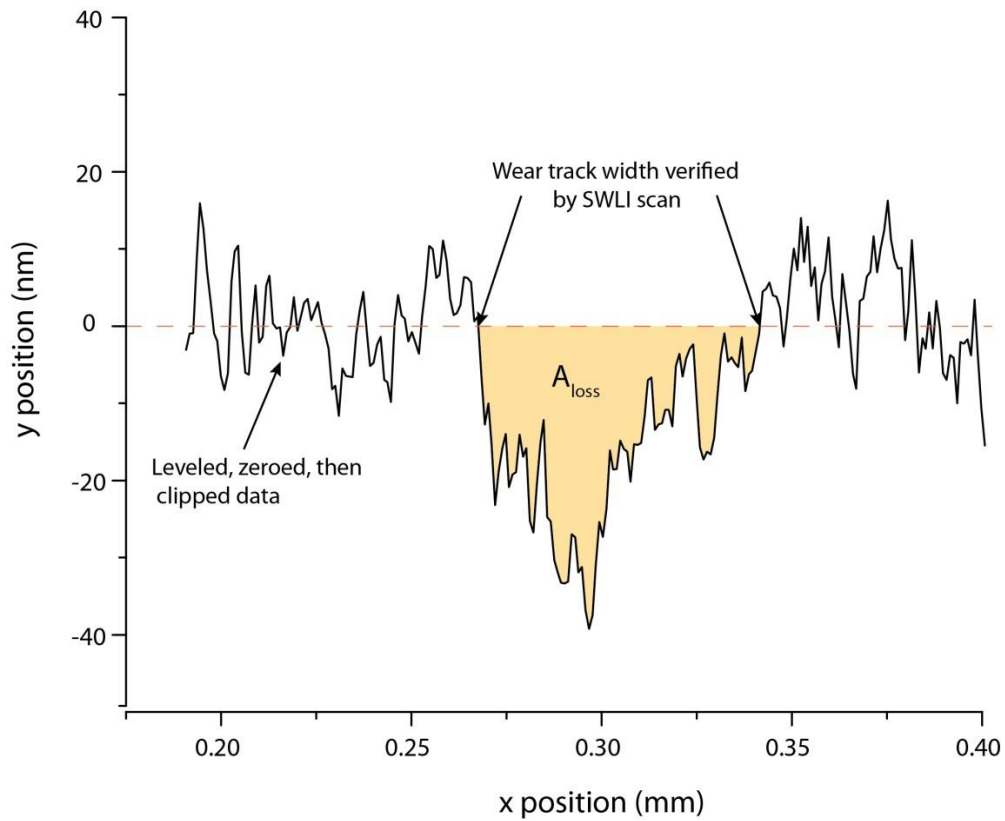


Figure 3-4. A typical cross-sectional profile of the wear track of MgO. Additionally, how area loss determinations were made.

Anisotropic wear behavior was found over a 3000 cycle wear experiment on a single crystal MgO specimen. The anisotropic trend can be seen below in Figure 3-5. From the figure, it is evident that the wear rate dependency on sliding speed is manifested by a sinusoidal wave of $\frac{\pi}{2}$ periodicity. The wear rate data is fitted with a sinusoid that is centered about $7.73 \times 10^{-7} \text{ mm}^3/\text{Nm}$ with peak to peak values ranging from as high $1.16 \times 10^{-7} \text{ mm}^3/\text{Nm}$ down to $3.90 \times 10^{-7} \text{ mm}^3/\text{Nm}$.

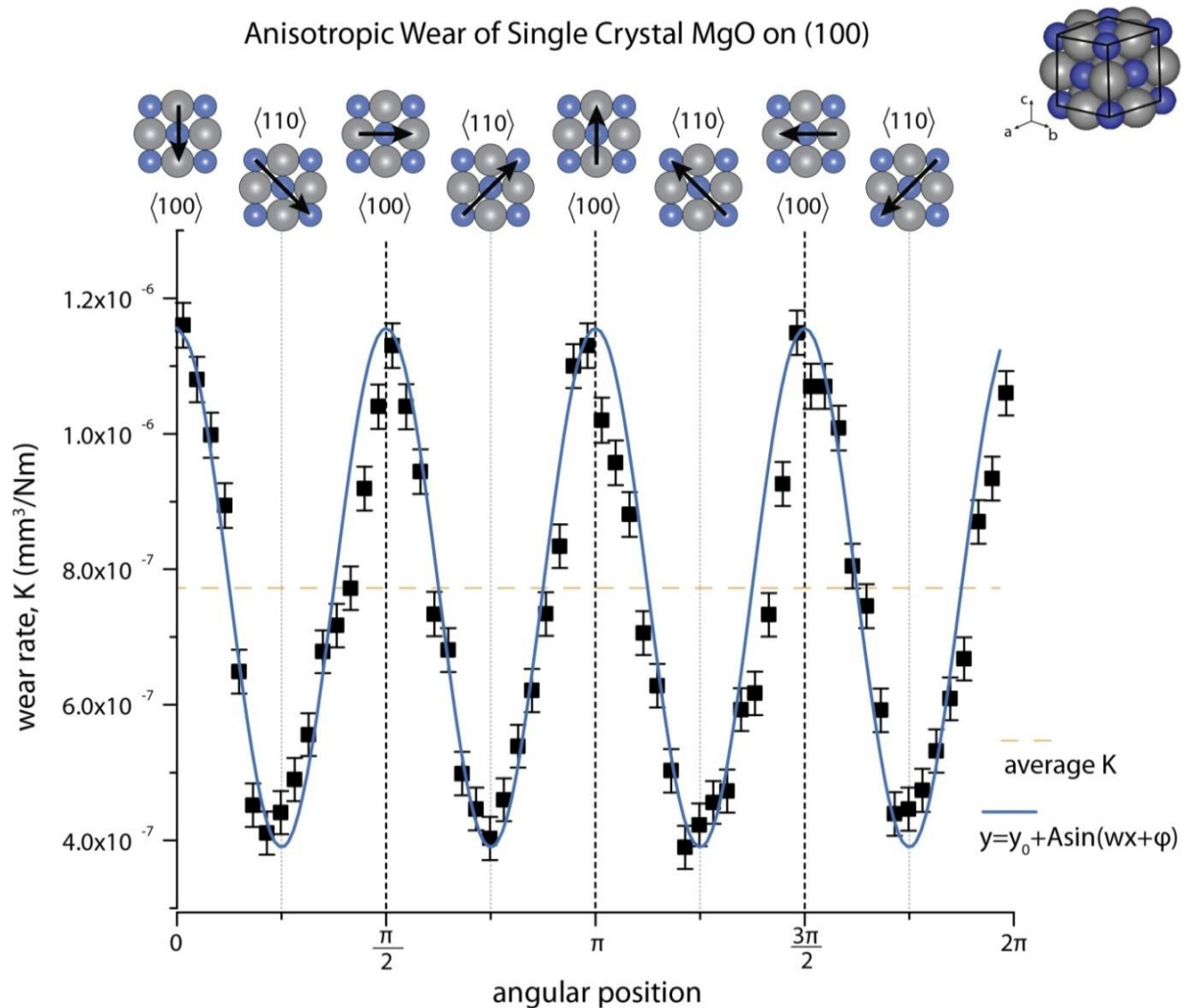


Figure 3-5. Anisotropic wear behavior of single crystal MgO expressed as a function of the angular position, measured from the center of the wear track. The black arrows represent the family of sliding direction at that position. Directions were verified by LEED.

The specific crystallographic sliding directions above are based on a low energy electron diffraction (LEED) analysis. The LEED analysis provides crystallographic orientation by using electron diffraction patterns. The results of the analysis showed that the $\langle 110 \rangle$ direction was approximately 23° from wear track tangential direction at the assigned 0° position. Knowing that the $\langle 110 \rangle$ and $\langle 100 \rangle$ directions must be separated by 45° , the data were examined and it was verified that the direction notations above are indeed correct.

The magnitudes of the wear rates seen above in Figure 3-5 are representative of a low wearing solid. The wear resistance strength of MgO can be attributed to numerous crystal-chemical properties. With large electronegativity differences between magnesium and oxygen, the strength of the ionic bonding is high. This also correlates to a high percent ionicity of approximately 68% [28]. The ionic potential is an important property of an ionic solid as it describes the charge density at the surface of the ion. It also provides a sense of how strongly an ion will be electrostatically attracted to ions of opposite charge or repelled by ions of like charge. The ionic potential as described by Erdemir [29] is the ratio of the cationic charge to the cationic radius. For MgO, the ionic potential is calculated as approximately 2.8, whereas for a similar structured 1(+), 1(-) sodium chloride, the ionic potential is much less at approximately 0.98.

Determined in previous studies¹, the activation energy (expressed in eV) necessary to displace an ion from its lattice position to an interstitial site (a Frenkel defect) is of great importance to understanding how strong the ionic bonds are. This

¹ W.G Sawyer, B. A. Krick, K. R. Marchman, Unpublished Ionic Solid Wear, 2011.

potential energy can be calculated using Coulomb's law and a geometrical surface constant based on Madelung's method as shown below in equation (3-5).

$$U = \frac{e^2 q \sum M_s}{4\pi\epsilon_0} \quad (3-5)$$

In the above, e is the charge of an electron (1.6022×10^{-19} C), q is the magnitude of the ion's charge, and $\frac{1}{4\pi\epsilon_0}$ is Coulomb's constant (8.98755×10^9 J m/C²). The term M_s represents a geometrical surface constant based on Madelung's method. This constant represents the amount of energy necessary to remove an anion or cation from the surface based on the closeness of its nearest neighbors. This value was found using a summation of neighbors in square loops radiating from the ion of interest. It was determined that the contribution to the total energy would converge around five loops away from the ion of interest. For MgO it was found that this activation energy was high at around 40 eV, indicating a strong bonding nature of the surface.

To gain an understanding of why the wear rate varies with crystallographic directions, it is important to examine the resolved shear stresses and how they are distributed along the slip planes. The slip systems of MgO are well known and occur at $\{110\} \langle 110 \rangle$ orientations [11, 15, 16, 18]. In this slip system, there are six slip planes in total; there are four slip planes that are at a 45° angle from the cube surface ($\{100\}$ planes) and two that are 90° from the cube surface. Three of the six slip planes are shown in Figure 3-6.

In his studies with MgO as discussed previously, Bowden determined that the shear stresses due to sliding differ substantially from the $\langle 100 \rangle$ directions and the $\langle 110 \rangle$ directions. The resolved shear stress on a slip plane can be defined as

$$\tau = \sigma \cos \alpha \cos \lambda \quad (3-6)$$

where σ is the applied stress, α is the angle between the resultant stress axis and the slip plane normal, and λ is the angle between the resultant stress axis and the slip direction.

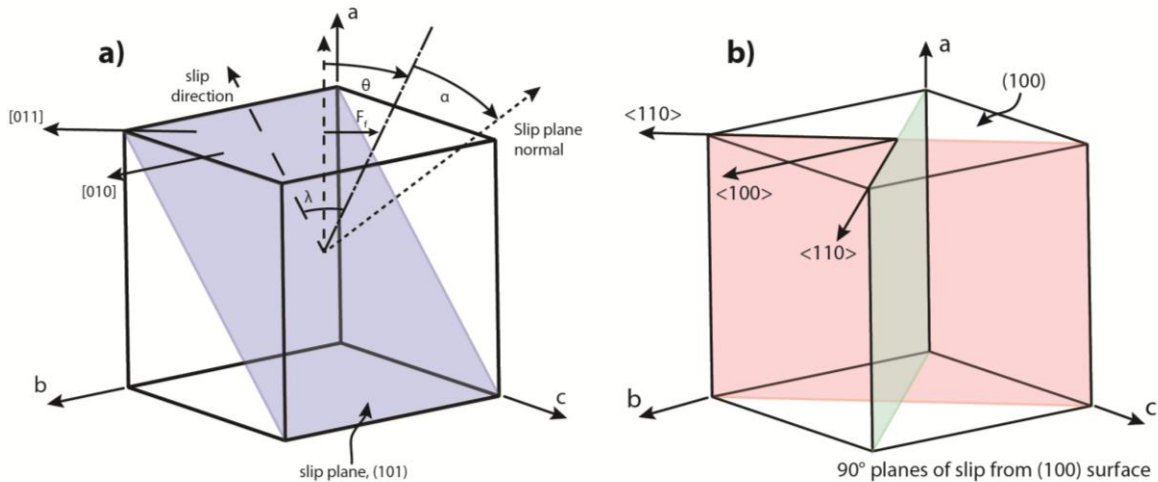


Figure 3-6. Slip plane notations. a) nomenclature used for resolved shear stress calculations. b) the slip planes at 90° from the (100) surface

By using the notation depicted above in Figure 3-6, the resolved shearing stresses can be determined. A more detailed solution to this problem is found in Appendix B: Resolved Shear Stress Calculations. From the calculations it is evident that the shear stresses differ substantially on which way the friction force vector is oriented (i.e. the sliding direction). Since the friction coefficient was mostly uniform around the wear track as shown above, the force vector as seen in Figure 3-6 was held constant throughout its sweep. Based on the analysis, when sliding in the $\langle 100 \rangle$ directions the shear stress is mostly carried by only two of the four 45° planes. These are the planes

that intersect the surface perpendicular to the direction of sliding. Also, the shear stress is approximately two times the magnitude of that in the $\langle 110 \rangle$ directions. When sliding in the $\langle 110 \rangle$ directions the shear stresses are more evenly distributed over all four of the 45° slip planes. The two slip planes that intersect the surface at 90° bear no shearing stress for any of the directions. Due to the higher magnitude of shear stresses, and being more concentrated, we would expect to see higher wear in those directions. The resolved shear stresses plotted against an angular sweep on the (100) surface is shown below in Figure 3-7.

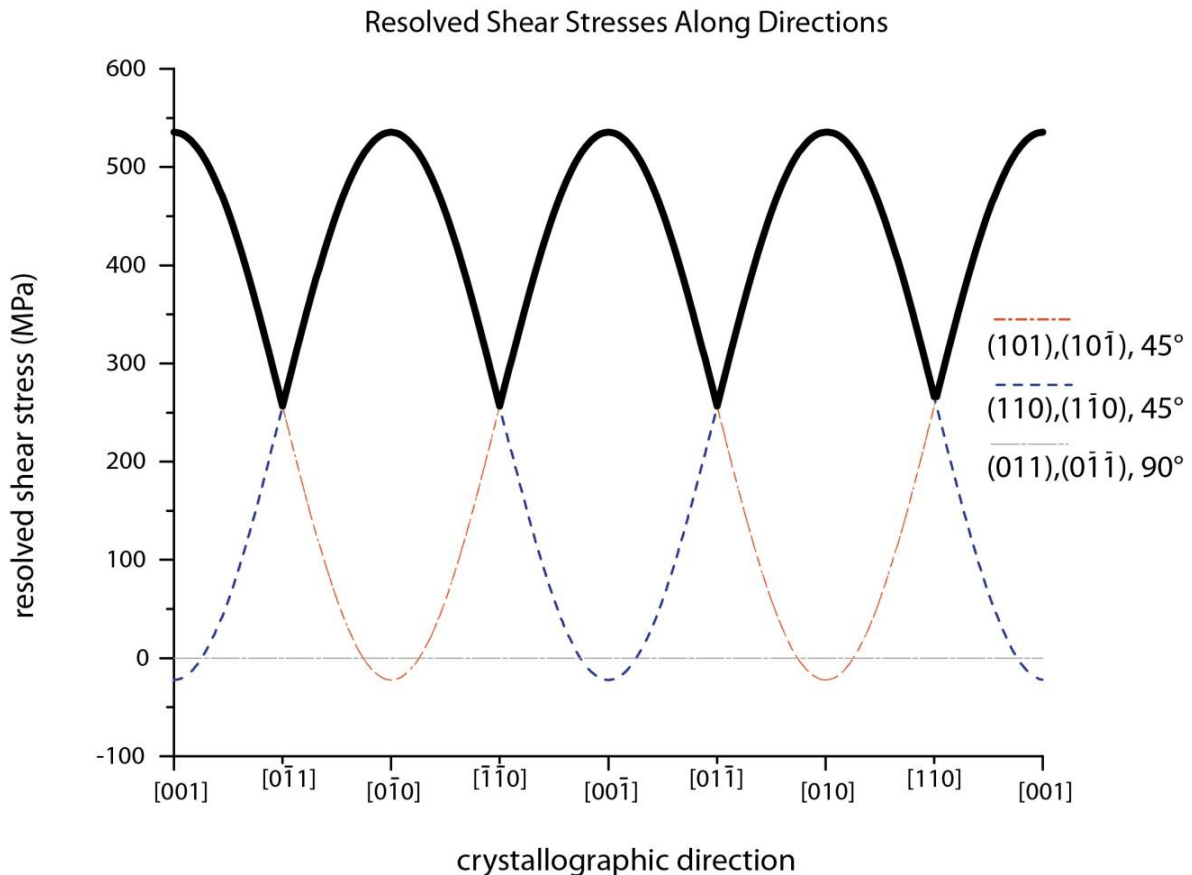


Figure 3-7. The resolved shear stresses as a function of sliding direction on the (100) plane. The solid path represents the magnitude between the different slip planes. This trend follows perfectly with the wear rate trend seen above.

The large dislocations observed by numerous previous studies on MgO typically manifest themselves as chevron type cracks emanating from the wear track. This cracking is a result of both high load and sliding distance. In order to obtain a wear track that produces accurate area loss data, this realm of plastic deformation was avoided. Wear studies and measurements were only carried out prior to this severe cracking. In Figure 3-8 a before and after micrograph of the wear track shows how the sample can go from little plastic deformation to severe plastic deformation in a span of ~700 cycles.

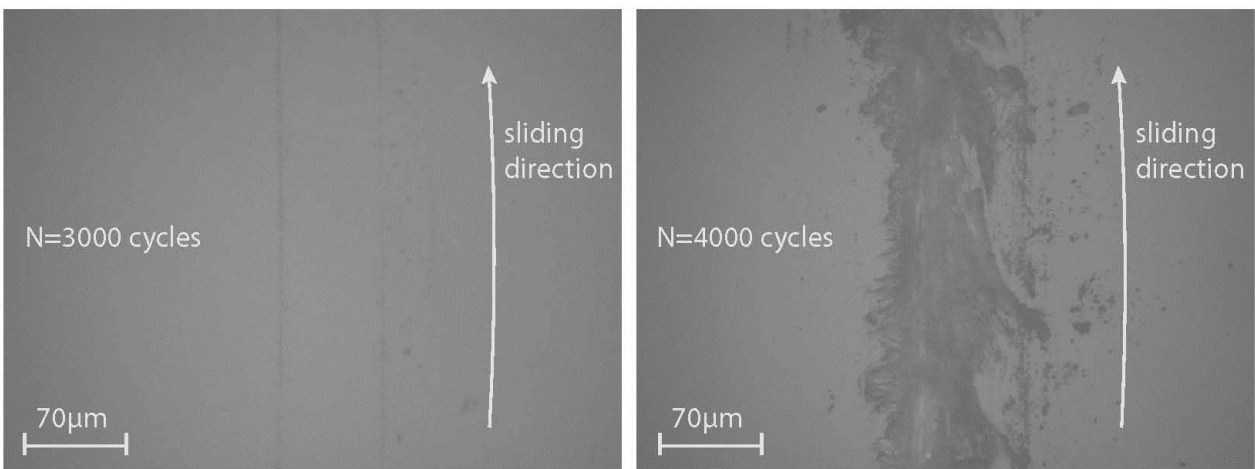


Figure 3-8. The severity of the plastic deformation rapidly increases over a relatively short period of sliding. The cracks began to propagate at approximately 3700 cycles.

Alongside the MgO wear testing, two other comparative tests were run to validate the effect of crystallographic sliding direction on wear rates. Sodium chloride (NaCl) is of the same structure as MgO but has ionic charges of 1(+), 1(-). Based on the trend found in MgO, the NaCl wear rates should follow suit. The expected difference is that the wear rate magnitude will increase by at least a couple orders of magnitude. To test the trend in the opposite direction, a control test was administered on amorphous soda-lime

glass. The experimental procedures for the MgO experiment were followed precisely for these two comparative tests. The results for this set of tests are reported in Figure 3-9 below.

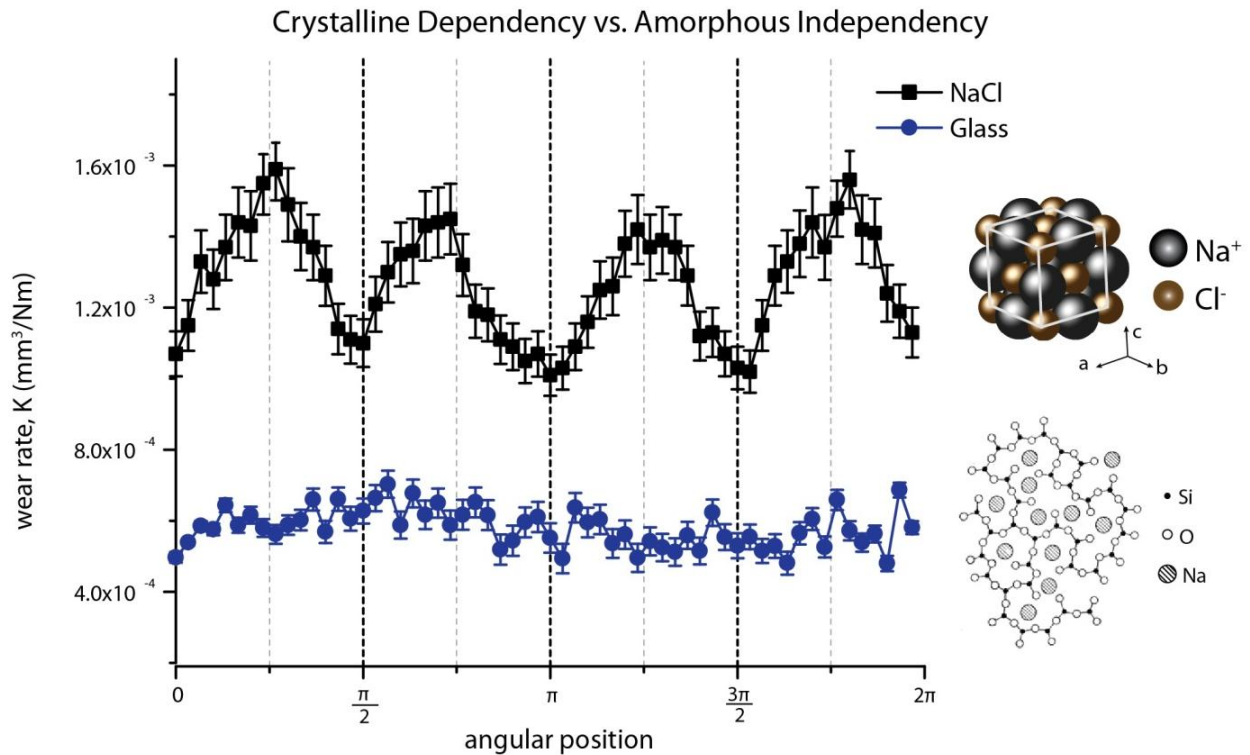


Figure 3-9. A comparative and control test to the MgO results above. The ionic crystalline structure produces similar dependency results while the amorphous glass shows constant wear.

The orientation for the NaCl crystal in the above data is not well defined at this point as it was for MgO. Currently, LEED data is being taken for future studies. It is evident, however that the trend is still there and the crystallographic directions are expected to match those defined for MgO.

CHAPTER 4 CONCLUSIONS

A novel pin-on-disk tribometer was fitted to a scanning white light interferometer for an *in situ* approach at wear monitoring of single crystal magnesium oxide. The objective of this work was to determine if single crystal magnesium oxide would wear dependently on the crystallographic sliding direction. To validate the measurements taken, the combined standard uncertainties were determined and were on the order of a few percent. Using six degree scan increments for a total of 60 data points, the wear volume was calculated. The wear rates showed a strong crystallographic sliding direction dependency that is not induced by a varying normal force. This suggests that there is some sort of mechanical or atomically energetic process that explains the anisotropic wear behavior. It is suggested that the resolved shear stresses on the slip planes are substantially different when sliding the $\langle 100 \rangle$ and $\langle 110 \rangle$ directions. In fact, it was found that when sliding in the $\langle 110 \rangle$ directions, the shear stress acting on the active slip planes was half the magnitude of that when sliding in the $\langle 100 \rangle$ directions.

APPENDIX A UNCERTAINTY ANALYSIS

The combined standard uncertainty of a measured value can be found by applying the law of propagation of uncertainty, shown below in equation (3-4) (A-1). The combined standard uncertainty represents one standard deviation of the wear rate measurement.

$$u_c(R)^2 = \left(\frac{\partial R}{\partial x_1} u(x_1) \right)^2 + \left(\frac{\partial R}{\partial x_2} u(x_2) \right)^2 + \dots + \left(\frac{\partial R}{\partial x_n} u(x_n) \right)^2 \quad (3-5)(A-1)$$

This root sum square method incorporates the partials of the measurement value's equation, R, with respect to each of R's measurement components and their associated uncertainties.

Uncertainty in Coefficient of Friction Measurements

Equation (A-1) can be applied to equation (3-1) in order to determine the uncertainty in the friction force measurement.

$$u_c(\mu) = \left[\left(\frac{\partial \mu}{\partial F_N} u(F_N) \right)^2 + \left(\frac{\partial \mu}{\partial F_f} u(F_T) \right)^2 \right]^{\frac{1}{2}} \quad (A-2)$$

In order to determine the uncertainty in the F_N and F_f components, the root sum square method is then applied to equations (3-2) and (3-3). The combined standard uncertainty equations for the normal and tangential forces are

$$u_c(F_N) = \left[\left(\frac{\partial F_N}{\partial C_N} u(C_N) \right)^2 + \left(\frac{\partial F_N}{\partial V_N} u(V_N) \right)^2 \right]^{\frac{1}{2}} \quad (\text{A-3})$$

$$u_c(F_T) = \left[\left(\frac{\partial F_T}{\partial C_T} u(C_T) \right)^2 + \left(\frac{\partial F_T}{\partial V_T} u(V_T) \right)^2 \right]^{\frac{1}{2}} \quad (\text{A-4})$$

For the above equations, $u(C_N)$ and $u(C_T)$ are still unknown. These values are the uncertainties associated with the calibration constants in the normal and tangential directions. A subsequent application of the root sum square method to these parameters yielded calibration constant uncertainties of 7.3×10^{-3} and 1.7×10^{-2} N/V for the normal and tangential directions, respectively. The measured voltage uncertainties of the calibration sequence, V_N and V_T , scale as a function of the number of bits, n , that the data acquisition card possess and is equal to $\frac{1}{2^n}$. The card used in this study was a 16-bit card yielding an uncertainty in voltage readings of $15 \mu\text{V}$. The calculated uncertainty in the normal force based on the above equation was 0.005N . The fluctuation of the normal force, however, is approximately 0.025 N and therefore dominates over the calculated uncertainty value.

Along with the residual uncertainties associated with measurement parameters as discussed above, misalignment errors can be a large source of uncertainty as well. As described in [3], the error fraction for obtaining accurate friction coefficient measurements is a function of the angular misalignment of the normal and tangential force axes. Using a manufacturing tolerance misalignment angle less than 2° , as

discussed below, and an average friction coefficient of 0.2, the error fraction associated with the friction coefficient measurement was approximately 4%. Based on the pin misalignment nomenclature shown in Figure (A-1), the pin's misalignment angle, β , is less than 2° . The cosine uncertainty of the normal force due to normal direction misalignment then comes out to approximately 0.0001 N [6]. The largest contributor to the coefficient of friction measurement was found to be the friction force measurement itself. The results of the combined uncertainty analysis for friction coefficient measurements are summarized below in Table A-1.

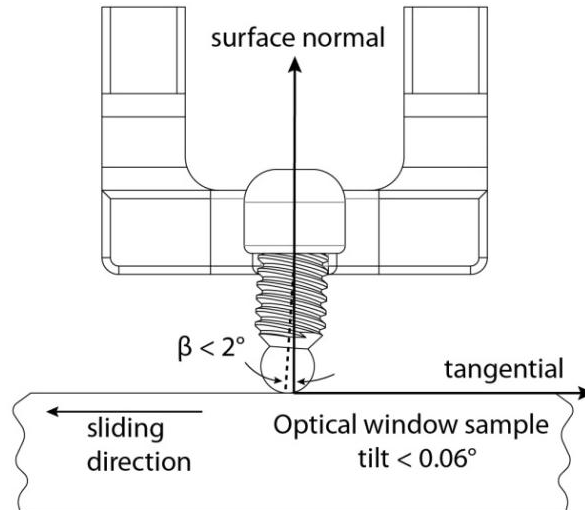


Figure A-1. Misalignment error in surface normal direction. Measured via optical techniques.

Uncertainty in Wear Rate Measurements

Wear rate measurements also incur uncertainties based on the components of the measurand, K . Applying equation (3-4) to equation (A-1) yields the combined standard uncertainty associated with the wear rate measurement:

$$u_c(K) = \left[\left(\frac{\partial K}{\partial V_{loss}} u(V_{loss}) \right)^2 + \left(\frac{\partial K}{\partial F_N} u(F_N) \right)^2 + \left(\frac{\partial K}{\partial d} u(d) \right)^2 \right]^{\frac{1}{2}} \quad (\text{A-5})$$

The method used here for determining the uncertainty in volume loss of the wear track was adopted from [8], which depends heavily on the number of cross sectional scans (N) used in the area measurements. The volume loss uncertainty also depends on the track diameter (D) and the standard deviation of the areas (σ_A).

$$u(V_{loss}) = \frac{\pi D}{\sqrt{N}} \sigma_A \quad (\text{A-6})$$

To minimize the uncertainty associated with the volume loss measurements, thus increasing the validity of the wear rate measurement, 60 total scans were taken around the wear track and analyzed for area loss. A depiction of the sample, wear track, and scan orientations are shown Figure 3-3.

The tilt of the sample in the tangential direction to the pin was determined from the SWLI scan to be approximately 0.06°. This value is small enough to neglect its effect on the overall sliding distance. Therefore, the uncertainty associated with the sliding distance, $u(d)$, is dominated by the uncertainty in the radius measurement. This measurement was made using a Veeco Dektak stylus profilometer, with X and Y axis resolutions of 0.01 μm . Due to the uncertainties involved in making area loss measurements, it was determined that the volume loss measurement was the largest contributor to the wear rate uncertainty. The combined uncertainties for the wear rate measurements are summarized in Table A-2.

Table A-1. Uncertainty analysis calculations for friction coefficient measurements

Parameter	Nominal Value	Standard uncertainty	Sensitivity,	Contribution
		$u(x)$	$\frac{\partial \mu}{\partial x}$	(%)
F_N (N)	1.01	0.025	0.20	5.65
F_T (N)	0.202	0.004	0.99	94.35
Combined standard uncertainty $u_c(\mu)$			4.0×10^{-3}	

Table A-2. Uncertainty analysis calculations for wear rate measurements of MgO

Parameter	Nominal Value	Standard uncertainty	Sensitivity,	Contribution
		$u(x)$	$\frac{\partial \mu}{\partial x}$	(%)
F_N (N)	1.01	0.025	0.20	25.34
V_{loss} (mm ³)	1.3×10^{-4}	5.61×10^{-6}	5.5×10^{-3}	74.65
d (m)	180	1×10^{-8}	4.08×10^{-9}	0
Combined standard uncertainty $u_c(K)$			3.6×10^{-8}	

friction force resultant R:

$$\hat{R} = \frac{F_N \hat{i} + \frac{\cos \theta}{F_f} - \frac{\sin \theta}{F_f}}{\sqrt{F_N^2 + \left(\frac{\cos \theta}{F_f}\right)^2 - \left(\frac{\sin \theta}{F_f}\right)^2}}$$

alpha α :

$$\alpha = \cos^{-1} \left(\frac{\frac{\cos \theta}{F_f} + F_N}{\sqrt{2} \sqrt{F_N^2 + \left(\frac{\cos \theta}{F_f}\right)^2 - \left(\frac{\sin \theta}{F_f}\right)^2}} \right)$$

lambda λ :

$$\lambda = \cos^{-1} \left(\frac{\frac{\cos \theta}{F_f} - F_N}{\sqrt{2} \sqrt{F_N^2 + \left(\frac{\cos \theta}{F_f}\right)^2 - \left(\frac{\sin \theta}{F_f}\right)^2}} \right)$$

resolved shear stress τ_r :

$$\tau_r = \sigma \cos \alpha \cos \lambda$$

LIST OF REFERENCES

1. Bhushan, B., *Contact mechanics of rough surfaces in tribology: multiple asperity contact*. Tribology Letters, 1998. **4**(1): p. 1-35.
2. Bowden, F.P. and D. Tabor, *Friction, lubrication and wear: a survey of work during the last decade*. British Journal of Applied Physics, 1966. **17**(12): p. 1521.
3. Schmitz, T.L., et al., *The Difficulty of Measuring Low Friction: Uncertainty Analysis for Friction Coefficient Measurements*. Journal of Tribology, 2005. **127**(3): p. 673-678.
4. Krick, B. and W. Sawyer, *A Little Analysis of Errors in Friction for Small Wear Tracks*. Tribology Letters, 2010. **39**(2): p. 221-222.
5. Archard, J.F. and W. Hirst, *The Wear of Metals under Unlubricated Conditions*. Proceedings of the Royal Society of London. Series A. Mathematical and Physical Sciences, 1956. **236**(1206): p. 397-410.
6. Schmitz, T.L., et al., *Wear-Rate Uncertainty Analysis*. Journal of Tribology, 2004. **126**(4): p. 802-808.
7. Guicciardi, S., et al., *On data dispersion in pin-on-disk wear tests*. Wear, 2002. **252**(11-12): p. 1001-1006.
8. Colbert, R., et al., *Uncertainty in Pin-on-Disk Wear Volume Measurements Using Surface Scanning Techniques*. Tribology Letters, 2011. **42**(1): p. 129-131.
9. Amateau, M.F. and J.W. Spretnak, *Plastic Deformation in Magnesium Oxide Crystals Subjected to Rolling and Contact Stresses*. Journal of Applied Physics, 1963. **34**(8): p. 2340-2345.
10. Stokes, R.J. and C.H. Li, *Dislocation configurations and the initiation of yielding in magnesium oxide*. Discussions of the Faraday Society, 1964. **38**: p. 233-242.
11. Stokes, R.J., *Microstructure and Mechanical Properties of Ceramics*, 1963, Office of Naval Research: Hopkins, Minnesota.
12. Steijn, R.P., *Sliding and Wear in Ionic Crystals*. Journal of Applied Physics, 1963. **34**(2): p. 419-428.
13. Chang, R., *Dislocation Relaxation Phenomena in Oxide Crystals*. Journal of Applied Physics, 1961. **32**(6): p. 1127-1132.

14. Washburn, J., et al., *Electron microscope observations of deformed magnesium oxide*. Philosophical Magazine, 1960. **5**(58): p. 991-999.
15. Sugita, T., K. Suzuki, and S. Kinoshita, *Wear characteristics of magnesium oxide single crystals on steel*. Wear, 1977. **45**(1): p. 57-73.
16. Dufrane, K.F. and W.A. Glaeser, *Rolling-contact deformation of MgO single crystals*. Wear, 1976. **37**(1): p. 21-32.
17. Bowden, F.P. and A.E. Hanwell, *The Friction of Clean Crystal Surfaces*. Proceedings of the Royal Society of London. Series A. Mathematical and Physical Sciences, 1966. **295**(1442): p. 233-243.
18. Bowden, F.P. and C.A. Brookes, *Frictional Anisotropy in Nonmetallic Crystals*. Proceedings of the Royal Society of London. Series A. Mathematical and Physical Sciences, 1966. **295**(1442): p. 244-258.
19. W. G. Sawyer, S.S.P., M. A. Hamilton, N. Argibay, L. A. Alvarez, N. Mauntler, A. A. Voevodin. *Wear Testing and In Situ Profilometry*. in *World Tribology Congress*. 2009.
20. Argibay, N., J.A. Bares, and W.G. Sawyer, *Asymmetric wear behavior of self-mated copper fiber brush and slip-ring sliding electrical contacts in a humid carbon dioxide environment*. Wear, 2010. **268**(3-4): p. 455-463.
21. K. Wahl, W.G.S., *Observing Interfacial Sliding Processes in Solid-Solid Contacts*. MRS Bulletin, 2008.
22. Wyant, J.C. *White light interferometry*. 2002. SPIE.
23. Kurganskaya, I. *The Application of VSI (Vertical Scanning Interferometry) to the Study of Crystal Surface Processes*. 2009 07/13/2009 [cited 2012 01/31/2012]; Available from: <http://cnx.org/content/m22326/latest/>.
24. Keith, J.H., *Design of a Pin-On-Disk Tribometer with In-Situ Optical Profilometry*, U.o. Florida, Editor 2010: Gainesville.
25. Krick, B. and W. Sawyer, *Space Tribometers: Design for Exposed Experiments on Orbit*. Tribology Letters, 2011. **41**(1): p. 303-311.
26. N. Mauntler, T.S., M. Hamilton, J. Steffens, N. Argibay, J. Bares, W.G. Sawyer, *Tribometers for In Situ Profilometry*, 2007.
27. Xu, L., H. Bluhm, and M. Salmeron, *An AFM study of the tribological properties of NaCl (100) surfaces under moist air*. Surface Science, 1998. **407**(1-3): p. 251-255.

28. E. W Bucholz, C.S.K., K. R. Marchman, W.G Sawyer, S. R Phillpot, S. B Sinnott, K. Rajan, *Data-driven Model for Estimation of Friction Coefficient via Informatics Methods*. Tribology Letters, 2012.
29. Erdemir, A., *A crystal-chemical approach to lubrication by solid oxides*. Tribology Letters, 2000. **8**(2): p. 97-102.

BIOGRAPHICAL SKETCH

Kellon Marchman was born in 1988 in Fort Walton Beach, Florida. He grew up in Niceville, Florida where he attended Niceville High School. He captained the NHS varsity soccer team his senior year in 2006. He continued his education at the University of Florida starting in the summer of 2006 where he was initially enrolled in nuclear engineering. After determining his passion, he switched to mechanical engineering where he remained and finished his undergraduate coursework in less than 4 years. He started undergraduate research in the University of Florida Tribology Laboratory under Professor W. Gregory Sawyer in the summer of 2009. He graduated with honors in the summer of 2010 with his Bachelor of Science degree in mechanical engineering. He remained in the Tribology Laboratory for his graduate studies where he attended and presented at numerous Society of Tribologists and Lubrication Engineers (STLE) conferences. His main graduate work was in the study of wear of mineralogical and ionic solids, however, he helped with numerous other studies. He graduated in the spring of 2012 with his Master of Science degree in mechanical engineering.